Mater Renew Sustain Energy (2015) 4:14
DOI 10.1007/s40243-015-0056-7

ORIGINAL PAPER

# Vacuum-sintered stainless steel porous supports for inkjet printing of functional SOFC coatings

**R. I. Tomov[1] · M. Krauz[2] · A. Tluczek[2] · R. Kluczowski[2] · Venkatesan V. Krishnan[3] · K. Balasubramanian[3] · R. V. Kumar[1] · B. A. Glowacki[1,4,5]**

Received: 7 May 2015 / Accepted: 14 July 2015 / Published online: 31 July 2015


**Abstract** Porous metal supports for SOFC applications were produced via conventional powder metallurgy routes—tape casting and high-pressure injection moulding. The supports were sintered in vacuum at different vacuum levels and temperatures. Commercially accessible low-cost stainless steel 430L powder was chosen as source material. The relations between the vacuum sintering temperature and the supports properties were studied. The density and the open porosity distribution of sintered supports were determined by Archimedes' method, Optical Image Analysis and Hg-porosimetry. The microstructure and the stainless steel grain surface composition evolution were investigated by scanning electron microscope and energy dispersive X-ray spectrometry. direct ceramic inkjet printing (DCIJP) was employed as coating technology for depositing anode (NiO/GDC) and electrolyte GDC coatings. Suspension anode and electrolyte inks were developed in-house and the printing procedure was optimized to produce uniform coatings with thicknesses below 15 µm. The analyses confirmed that the as-produced substrates were suitable to support DCIJP deposited SOFC functional coatings.

**Keywords** SOFC · Metal supports · Cell fabrication · Inkjet printing

✉ R. I. Tomov
rit21@cam.ac.uk

[1] Department of Materials Science and Metallurgy, University of Cambridge, 27 Charles Babbage Road, Cambridge CB3 0FS, UK

[2] Ceramic Department CEREL, Institute of Power Engineering, Boguchwała, Poland

[3] Non-Ferrous Materials Technology Development Center, Hyderabad, India

[4] Department of Physics and Energy, University of Limerick, Plassey, Ireland

[5] Institute of Power Engineering, Warsaw, Poland

## Introduction

Solid oxide fuel cells (SOFCs) have been object of continuous research efforts for decades due to their highly efficient direct conversion of chemical energy into electricity, fuel flexibility and environmental benefits. The SOFC cover wide range of applications including stationary (MW) and auxiliary (kW) power units, combined heat and power installations and decentralised off-grid applications. Depending on the design SOFCs can operate at temperatures within the region of 600–1000 °C [1, 2]. The state-of-the-art commercial SOFCs are based on a combination of cermet anodes (e.g. Ni–YSZ) and ion-conducting ceramic electrolyte materials, most often yttria-stabilized zirconia (8YSZ) or doped ceria (Gd:$CeO_2$). Both materials offer the required chemical and thermal stability in oxidizing and reducing atmospheres and good oxygen ionic conductivity over a wide range of conditions [3, 4]. The commonly used anode-supported SOFC design is based on porous cermets providing mechanical support and permeation path for the fuel and the reaction products. Ni–YSZ anodes are preferred due to their sufficient electrical conductivity and mechanical strength, as well as minimal chemical interaction with the electrolyte [5]. However, such supports having thicknesses of ~0.5–1.0 mm thickness can contribute significant cost due to the high-volume fraction of rare earth containing materials. In addition, the cermet electrodes are mechanically fragile and do not

sustain thermal shock stresses. The operating temperatures of SOFCs at levels of 800–1000 °C introduce further limitations in SOFCs fabrication and operation. Such temperatures require utilization of expensive corrosive resistant interconnects and are detrimental to the durability of the cell causing functional materials degradation. As a consequence, the main barriers for SOFCs commercialization have been recognized as the high cost of production and the operational durability. Currently a shift towards intermediate temperatures (<800 °C) is considered essential for the commercialization of SOFCs technology. The advantages of reduced-temperature operation also include systems design compactness and wider choice of materials [6]. The strategies for compensating the incurred drop in ionic conductivity include lowering the electrolyte resistance either by implementing thinner electrolyte or using higher ionic conductive materials as well as reduction of the potential interfacial polarization losses and enhancement of the electrochemical activity of the electrodes [7]. Lowering the operational temperature permits utilization of less expensive stainless steel as support and interconnector materials. Porous metal substrates with thicknesses of few hundreds of micrometers are advantageous for SOFCs since they provide good electrical conduction, high mechanical strength, favourable thermal distribution due to the high thermal conduction and as a consequence rapid start-up times [8–10]. Metal supported SOFCs can also enable conventional metal joining techniques in the stack assembly. Ferritic stainless steels offer well-matched thermal expansion coefficient (TEC) with commonly used ceramics ($TEC_{8YSZ} \sim 10.4$–$11.0\ ppmK^{-1}$, $TEC_{GDC} \sim 12.7\ ppmK^{-1}$, $TEC_{NiO/YSZ} \sim 12.3\ ppmK^{-1}$ for an NiO/YSZ composite with 53 vol %NiO and $TEC_{430L} \sim 11.4$ - $ppmK^{-1}$) which is beneficial for withstanding repeated thermal stresses caused by rapid thermal cycling [8–12].

One of the main obstacles for the use of metal supports at elevated temperatures is their corrosion. Partial oxygen pressures during SOFC operation can vary from values ~1 atm on the cathode side to values $\sim 10^{-20}$ atm on the anode side. Although the latter is a very low value it is thermodynamically in the metal oxide formation region. The problem can be partially resolved by the formation of $Cr_2O_3$ protective coating onto the metal scaffolding which effectively stops further degradation and retains good electrical conductivity. Variety of different ferritic steels and alloys have been studied for SOFCs applications including standard commercial 316 and 430 series and as well as more expensive specialized (higher Cr content) ones-Crofer22 APU (*ThyssenKrupp VDM*), E-Brite (Allegheny Ludlum), ZMG232 (Hitachi Metals Ltd.), FeCr (70:30) (AMETEK) and Ti-Nb stabilized 17 % Cr ferritic stainless steel used by CERES Power [8–10, 13, 14]. Some austenitic nickel-based alloys (Haynes 230 and Haynes 242-Haynes International) have also been experimented with. The higher percentage of chromium content promotes the formation of a protective scale but chromia is volatile under certain conditions and can degrade the performance of the cell. Thus, a number of protective coatings preventing the effects of Cr poisoning and depletion are currently under development [13, 14]. The corrosion resistance of 430 steel has been previously investigated in both cathode (air) and anode ($H_2$–$H_2O$) conditions at operational SOFC temperatures (750–900 °C). It was found that chromium content of ~16 at. % is not sufficient to form protective scale at cathode conditions. As a consequence, such metallic components are considered better employed on the anode side where rich hydrogen atmosphere is present [15–18].

Despite being patented almost half a century ago [19] the use of stainless steel metal supports in SOFCs became feasible in the recent years along with the development of commercially viable methods for integration of low-cost "wet" ceramic routes with the sintering procedures compatible with metallic supports [20]. The densification of the electrolyte layer normally performed at high sintering temperatures (above 1300 °C) requires protective atmosphere (e.g. $H_2$, Ar, vacuum) for the preservation of metal support integrity. At high temperatures, such treatment can lead to substantial and detrimental changes in the composition and microstructure of the stainless steel support. High purity of the shielding gas is required in order to prevent loss of Cr through formation of volatiles. Sintering and slow cooling in hydrogen can be potential causes for secondary phase's precipitation with negative effect on both the mechanical and corrosion properties and is associated with mandatory safety precautions and a high cost [21]. Vacuum sintering was reported to provide corrosion-resistant steel structures since there is no chromium depletion through the formation of chromium oxides or nitrides. This is due to the low stability of chromium oxide under vacuum conditions at temperatures exceeding 900 °C. As suggested by Bautista et al. [22] loss of Cr from vapourization can occur also during vacuum sintering and the probability of Cr vapourization increases with the rise of sintering temperature.

This study reports on the fabrication of metal supports for SOFCs by vacuum sintering and the evaluation of the porous substrates suitability for direct ceramic inkjet printing (DCIJP) of SOFC functional coatings. The "green" metal supports were produced by commercial powder metallurgy methods such as tape casting and high-pressure injection moulding. Commercially accessible stainless steel 430L powders were chosen as source supports material. The DCIJP technique is simple and cost-effective non-contact "wet" technique for fabrication of ceramic coatings onto variety of surfaces. It can reproducibly dispense droplets in the range of nL volumes at

high rates (kHz). Drop-on-demand (DOD) ceramic inkjet printing offers excellent thickness and uniformity control and introduces the possibility of printing 2D and 3D patterns as well as continuous coatings. Inkjet systems offer wide scale of application—from experimentation platforms working with customized inks, up to mass manufacturing systems that can print rapidly and competitively on industrial scale. The technology is cost effective and environmentally friendly through waste minimization of the expensive precursors. The influence of the major printing parameters was evaluated. The production of anodes and electrolyte coatings with a modified Domino print head was reported previously by Tomov et al. [23, 24] using suspension inks. Wang et al. [25] deposited GDC electrolytes on NiO–8YSZ cermet anodes using sol–gel-based precursor solutions. Sukeshini et al. [26] employed a DMP-2831 printer for the deposition of 8YSZ electrolyte layers, LSM–YSZ and LSM cathode layers on to NiO–8YSZ supports, reporting a maximum power density of 450 mW/cm$^2$ at 850 °C in hydrogen.

## Experimental

### Metal supports preparation

Stainless steel type 430L is one of the most widely used ferritic stainless steels. It combines good corrosion resistance and oxidation resistance up to 816 °C (in continuous use) with good mechanical properties. The bulk density and thermal conductivity are reported in the literature as 7.74 g/cm$^3$ and 26.3 W/m.K, respectively. Commercially available 430L low-carbon stainless steel powders (average particle size ~15 μm) from Alpha Aesar were used for the fabrication of porous metal supports.

*Tape casting (TC)*

For the preparation of metal supports via TC 430L stainless steel powder was milled together with 40 wt% PVB-based binder in a ball-mill for 24 h. Subsequently, the suspension was de-aerated for 24 h during slow speed milling step. The process was performed with manual type tape-caster in which the slurry was coated onto a Teflon carrier. Speed of casting was 3 cm/s and the gap between the "doctor blade" and the table surface was set to 2 mm. The "green" foil was dried for 24 h in ambient air conditions.

*High-pressure injection moulding (HPIM)*

For the preparation of metal supports via HPIM stainless steel powders and 10 wt% thermoplastic binder (Zschimmer & Schwarz) were mixed with a mechanical stirrer in a heated chamber kept at a temperature of 110 °C. This mixture was then granulized using a pellets production set-up consisting of two counter screw compounders (Thermo Fisher), a cooling bath and a pelletizer (CEREL). The metal supports were produced by the following injection setting parameters: moulding temperature: 120 °C, mould temperature: 40 °C and moulding pressure: 1700 bar. The injection was done in a horizontal direction by means of two-part water cooled moulds made of hardened tool steel. The obtained "green" substrates were 62 × 62 mm$^2$ in size.

Circular shapes were produced by laser cutting of both TC and HPIM "green" tapes. The sintering of as-prepared green samples was carried out in a vacuum furnace equipped with rotary and oil diffusion pumps. The solvents and the binders were removed in situ during the thermal cycle. The relations between the sintering temperature and the metal supports composition, porosity, density and shrinkage were studied. The density and the open porosity of were determined by Archimedes' method employing water as sealant material as well as by optical image analysis (ImageJ software-J) of fractured surfaces. The porosity size distribution was evaluated with Hg-porosimetry using Micromeritics AutoPore IV 9500 system. The microstructure of the samples after sintering was investigated by inspection of fractured cells in scanning electron microscope (SEM) equipped with an energy dispersive X-ray spectrometry system (EDS). The micro-analyses were realized at ~10 mm working distance. Thermogravimetric analysis (TGA) was performed on the green tapes to evaluate the burn-out of the organic compounds and to design a suitable heat treatment procedure. Nitrogen gas at 100 mL/min was used as a shield gas simulating protective sintering environment. The temperature was ramped from room temperature to 1300 °C at 20 °C/min.

### Functional coatings deposition by DCIJP

The deposition process of the anode and the electrolyte on selected porous supports was done by DCIJP. The printer developed for the experiment consisted of an electromagnetically driven print head with 100-μm ruby nozzle orifice and x–y planar positioning system. An electromagnetic technology was chosen because it offers simplicity and reliability of use, as well as wider range of ink/suspension compatibility. This is an important advantage in comparison to piezoelectric inkjet heads which have either stringent requirements towards ink rheology or have to be designed specifically for a certain type of ink. The printer works on a magnetic piston/solenoid mechanism where the suspension ink is loaded into the reservoir and a pressure is applied onto it. The substrate is placed ~5 mm below the

nozzle orifice. As an electrical pulse controlled by the computer interface passes through the solenoid, the electromagnetic field lifts the piston off the surface of the nozzle for a certain amount of time—"open time" parameter. The pressure exerted onto the reservoir then forces a set amount of suspension ink through the nozzle dispensing a drop. The preparation of stable suspension inks is of critical importance for achieving repeatable jetting. The commercial NiO (Sigma Aldrich) and Gd:$CeO_2$-GDC (Fuel Cell Materials) powders were mixed with alpha-Terpineol and binders, and ball milled with 3YSZ beads in 3YSZ bowls in a planetary mill (Pulverisette, Fritsch, Germany). The mass load of the ceramic powders and the type of the ink carrier were limited by the rheological working window of the nozzle, which defined the regime of stable repeatable jetting. Hence, the viscosity of the suspension inks had to be adjusted to suitable levels by adding lower viscosity solvents–methanol (MeOH) or 1-Propanol (PrOH). The suspension inks developed were sufficiently stable to permit printing without mechanical agitation within 24 h of preparation. In order to minimize the risk of clogging of the nozzle care was taken to limit the particle size to below the empirically established level of 3 μm. The inks were filtered through 3-μm glass microfibre filters before being loaded into the nozzle compartments. The nozzles were observed to execute reproducible DOD tasks without clogging the internal fluidic pathways of the assembly.

## Results and discussion

### Stainless steel supports characterization

The TGA graphs shown in Fig. 1 suggested that solvent and binder additives to the TC and HPIM green samples were decomposing in the 200–500 °C temperature range. Further heating led to gradual oxidation of the stainless steel due to the residual oxygen in the shielding nitrogen gas becoming substantial above 800 °C. The mass loss observed at temperature above 1000 °C is most likely due to carbon residue content removal via oxidation and formation of volatile cromia. Based on the TGA results a heat treatment procedure suitable for both types of green supports was designed as follows: an initial solvent removal step at 240 °C was reached at a heating rate of 1 °C/min. Then the samples were heated at a rate of 1 °C/min up to 500 °C for a hold time of 2 h to complete the removal of the binders. Subsequently, the temperature was ramped at a rate of 2 °C/min to the final sintering temperature. The samples were cooled to room temperature at a ramp rate of 5 °C/min. The supports fabricated by both TC and HPIM methods were sintered in vacuum following the thermal

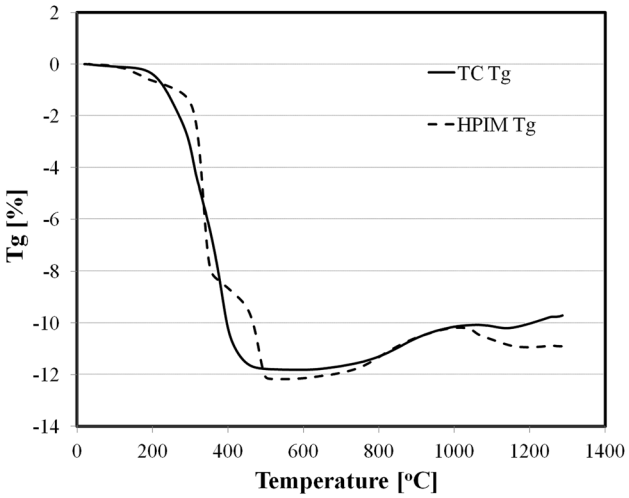


**Fig. 1** TGA *curves* of TC and HPIM green tapes in nitrogen

cycle described above in order to avoid formation of non-reducible oxide phases. The top surfaces of both types of supports had similar morphology without obvious macro-defects (see Fig. 2) and had sufficient flatness and mechanical strength for the subsequent integration of SOFCs functional coatings. Relative shrinkage calculated by comparing the initial diameter of the laser cut "green" supports with the diameter measured after the sintering at 1000 °C was in the range of 4.7–5.5 % for HPIM samples and 4.5–8.0 % for TC samples. As reported previously by Molin et al. [16] sintering of stainless steel porous substrates produced mechanically rigid supports at temperatures above 900 °C and grain necking was not observed below this temperature. Figure 3a–d display lower and higher magnification SEM images of fractured HPIM (Fig. 3a, c) and TC (Fig. 3b, d) supports sintered in vacuum at 1000 °C which revealed similar porous microstructure and evidence of grain necking.

Fractured supports sintered at two vacuum levels and two different temperatures were studied by EDS micro-analysis in order to evaluate the evolution of the elemental concentration on the stainless steel grain surfaces during the heat treatment procedure. The compositional analyses of the weight ratios of Cr/Fe and Si/Fe are presented in Table 1. The utilized technique did not allow accurate quantification of oxygen in order to illustrate the effectiveness of the vacuum as protective environment at different vacuum levels. The area probing results summarized in Table 1 revealed that the range of Cr enrichment measured on the stainless steel grains surfaces exceed Cr/Fe wt% ratio of 0.22 for both TC and HPIM supports and was found to be more pronounced at deeper vacuum conditions. Enhanced Si surface enrichment was observed at $2 \times 10^{-2}$ mbar vacuum as a result of silicon upward diffusion. Higher resolution imaging of individual grains presented in

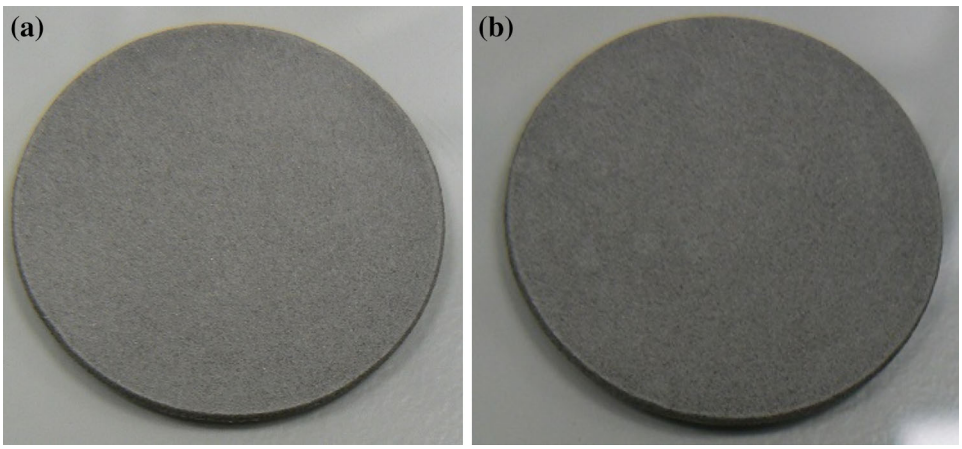


**Fig. 2** Optical images of stainless steel 430L metal supports prepared by (**a**) tape casting—TC and (**b**) injection moulding—IM and sintered in vacuum at 1000 °C

Fig. 3e demonstrated the formation of Cr-rich (Cr/Fe = 0.71—see area A) "skin"-type layer and Cr depletion detected underneath (Cr/Fe = 0.15—see area B). The increase of the sintering temperature to 1300 °C (see Fig. 3f) led to a loss of the open porosity accompanied by a relative reduction of Cr enrichment level and an increase in the density of Si precipitations.

The open porosity data of as-sintered supports is summarized in Fig. 4. The average open porosity above 40 % was measured for both types of supports sintered in vacuum at 1000 °C. The HPIM samples showed higher density (HPIM—4.33 g/cm$^3$ vs. TC—3.28 g/cm$^3$ at 1000 °C) and lower average open porosity mainly as a result of the lower mass loading of organic additives in the feedstock compared to the tape casting slurry. As expected, the density of all samples increased with the sintering temperature (HPIM—6.81 g/cm$^3$; TC—6.65 g/cm$^3$ at 1300 °C). The open porosity was practically non-existent in the supports sintered at 1300 °C. Open porosity level was estimated also from the SEM's images of fractured supports' surfaces processed by means of the Image J software through analysis of the image contrasts differences. This method produced similar results to the ones obtained by Archimedes' method (see Fig. 4). Figure 5 shows a typical plot of the relative and cumulative pore size distributions of an HPIM support sintered at 1000 °C in vacuum evaluated by mercury porosymetry. The peak on the right, corresponding to the intrusion in the range 30-200 μm, represents the penetration of the mercury into the vessels. Further peaks indicate multi-modal pore size distribution consisting of portions of larger interstitial pores (in the range of 7–15 μm) and majority of smaller pores with median pore radius of 2.6 μm comprising ~53 % of the open porosity. The overall value of the measured open porosity was 36.7 % and the skeletal density was evaluated at 6.53 g/cm$^3$. The result reflects the partially sintered state of the 430L stainless steel supports where the wide pore volume distribution was due to the broad starting particle size distribution of stainless steel powder with average particle size of ~15 μm. The inspection of the SS430L supports after sintering revealed small degree of warping and surface waviness. Hence the use of traditional ceramic coating techniques as screen printing was considered challenging. Thus coating technique insensitive to such degree of non-uniformity was employed, namely DCIJP.

## Suspension inks optimization

Analyses of particle size distribution of GDC and NiO suspension inks vs ball milling time is presented in Fig. 6. The inks milled for 4 h showed substantial broad tail beyond 3 μm nozzle limit. Extending the milling time to a minimum of 10 h led to a suitable sharper bi- and tri-modal distributions below the nozzle limit with $d(0.5) = 0.129$ μm for GDC ink and $d(0.5) = 0.443$ μm for NiO ink. The viscosities of the two separate NiO and GDC inks prepared by dilution in MeOH and PrOH were measured as 6.0–8.0 mPa.s for GDC and 7.0–8.5 mPa.s for NiO. Mixing NiO and GDC into a single anode ink lead to a small increase of viscosity (8.0–9.5 mPa.s) due to partial agglomeration during the mixing procedure.

## Jetting optimization

The behavior of the inks jetted through a print-head nozzle can be described with the help of the Reynolds (*Re*), Weber (*We*) and Ohnesorge (*Oh*) numbers—$Re = \upsilon\rho a/\eta$; $We = \upsilon^2\rho a/\gamma$; $Oh = (We)^{0.5}/Re = \eta/(a\rho\gamma)^{0.5}$ where $\rho$, $\eta$ and $\gamma$ are the density, dynamic viscosity and surface tension of the fluid, respectively, $\upsilon$ is the velocity and $a$ is a characteristic length. Printing of ceramic suspension inks has been an object of large number of studies in recent years. B. Derby summarized the research on the stability limits for DOD printing (ink printability, energy formation and

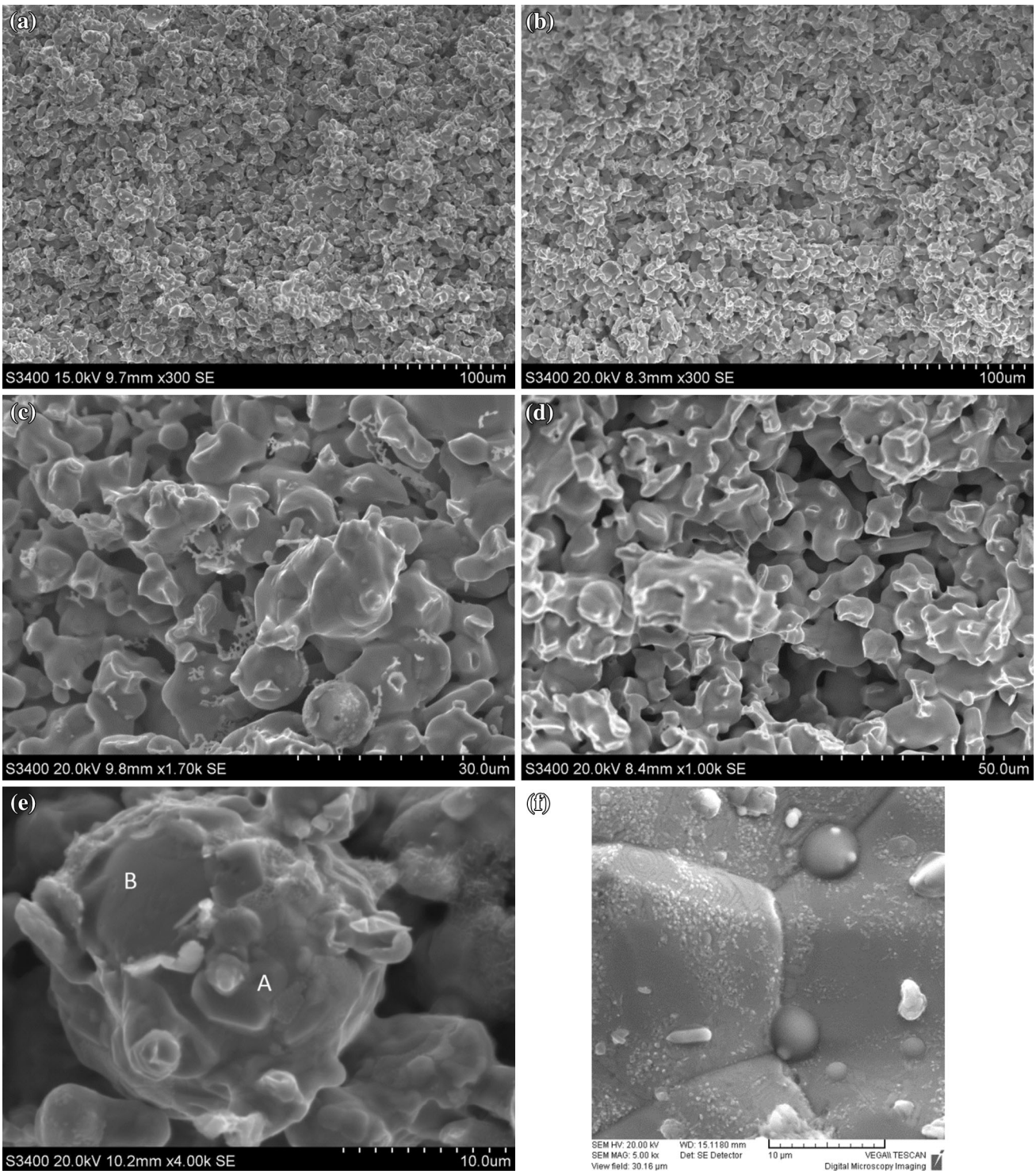


**Fig. 3** SEM image of fractured surfaces of HPIM (**a** and **c**) and TC (**b**, **d** and **e**) supports sintered in vacuum at 1000 °C and TC support sintered in vacuum at 1300 °C

splashing onset) in several review papers [27, 28]. The *Oh* number was identified as a suitable grouping of the ink physical constants characterizing drop generation. The conditions leading to stable jetting without formation of satellite drops were suggested as $10 > Z > 1$ (where $Z = 1/Oh$). Avoidance of delayed satellite drops formation is essential for achieving the desired thickness control of the coating. The study of the "energy of drop formation" limit

**Table 1** Compositional analysis of fractured surfaces of stainless steel TC and HPIM supports sintered at 1000 and 1300 °C in vacuum

| | Sintering temperature (°C) | Vacuum (mbar) | wt% ratio (Cr/Fe) | wt% ratio (Si/Fe) |
|---|---|---|---|---|
| Original SS-430L powder | na | na | 0.198 | <0.006 |
| TC and HPIM supports | 1000 | $2 \times 10^{-2}$ | 0.239–0.253 | 0.015–0.035 |
| | | $2 \times 10^{-5}$ | 0.281–0.298 | 0.007–0.011 |
| | 1300 | $2 \times 10^{-5}$ | 0.224–0.232 | 0.008–0.013 |

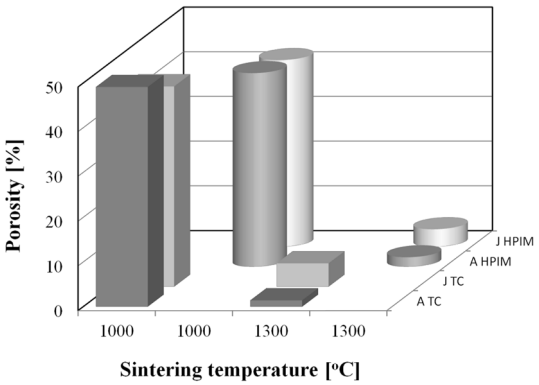


**Fig. 4** Open porosity of TC and HPIM supports sintered at 1000 and 1300 °C as measured by Archimedes' method (A) and evaluated with Image J software (J)

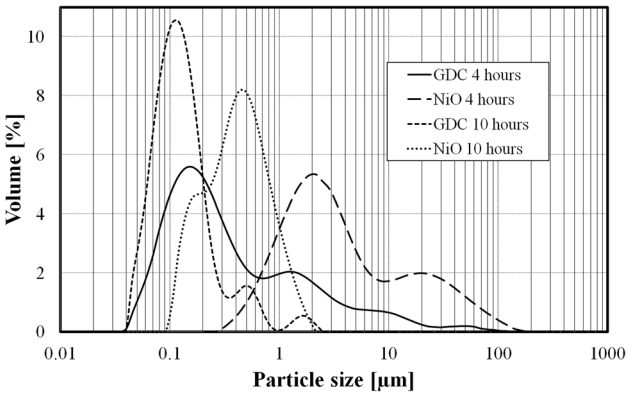


**Fig. 6** Particle size distribution of GDC and NiO ink diluted with methanol

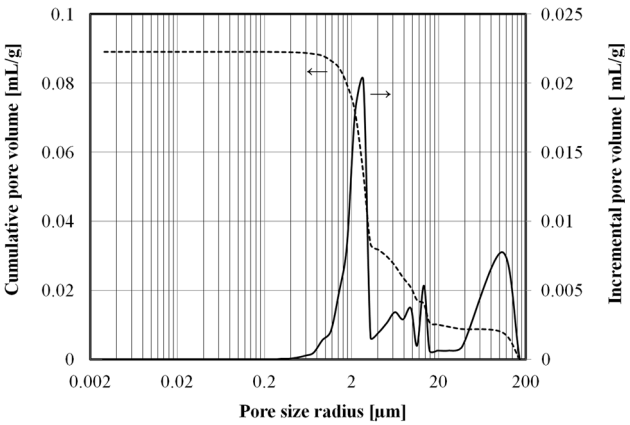


**Fig. 5** Pore size distribution of HPIM SS430L support sintered at 1000 °C in vacuum measured by mercury porosimetry

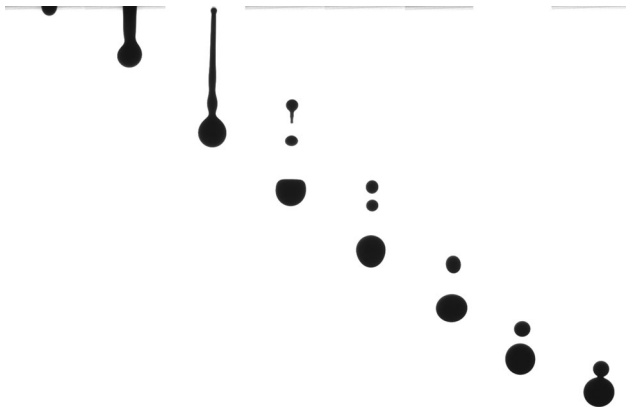

**Fig. 7** Drop visualization images of NiO–GDC–MeOH suspension ink jetted under a pressure of 350 mbar and 250 µs opening time

($We > 4$) and the "onset of splashing" limit ($We^{1/2}Re^{1/4} > 50$) requires precise knowledge of the drop velocity and the drop volumes characteristic for the particular printing system. The use of an integrated drop visualization system allowed us to examine in situ the drop volumes and velocities and to access the optimum printing parameters window. Such optimization for the electromagnetic print heads is based on the variation of carrier/solvent ratios, opening times and nozzle pressures. Figure 7 illustrates optimized drop formation behaviour of NiO–GDC–MeOH suspension ink jetted under a pressure of 300 mbar and 350 µs opening time. The initial drop breaks into a main drop and one or more smaller drops after it is detached from the nozzle. For optimized printing parameters the smaller drops soon merges with the main drop and forms back into a single drop. The information concerning measured velocities and released drop volumes is presented in Figs. 8 and 9. The same optimization was performed also for NiO–GDC–1-PrOH and GDC (MeOH, 1-PrOH) suspension inks. Based on the drop visualization results stable jetting was found to

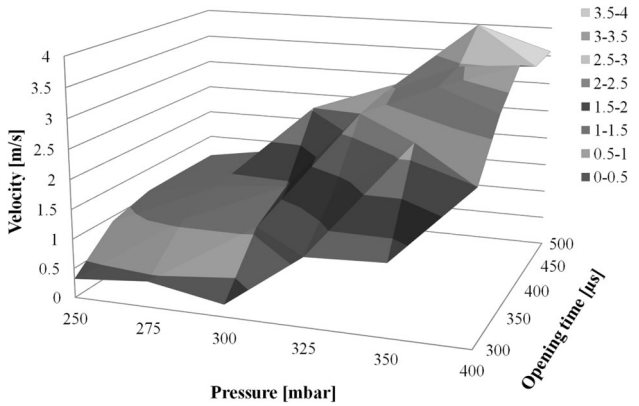


**Fig. 8** Drops velocity data from the visualization system showing jetting of NiO–GDC–MeOH suspension ink

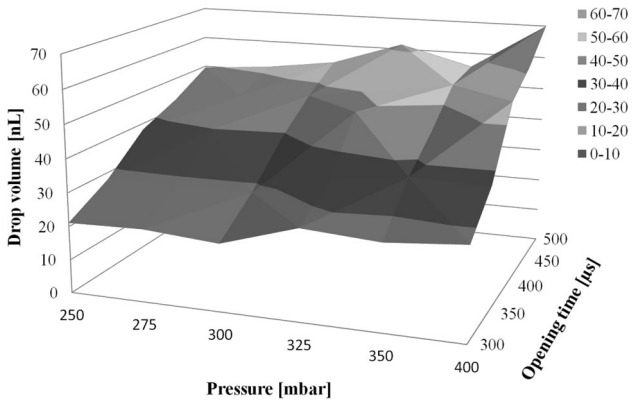


**Fig. 9** Calculated drop volumes versus pressure for NiO–GDC–MeOH suspension ink

relate to Z $\sim$ 7–8 for the inks developed. For the optimized printing parameters windows $We > 6$ and maximum $We^{1/2}Re^{1/4} = 11$ were estimated.

## Drop spreading optimization

Spreading and permeation of a droplet impinging on a porous substrate is a complex phenomenon driven by the porous medium parameters (porosity, particle size distribution) and the liquid drop properties (*Re, We*). The high axial momentum of the droplets jetted from the nozzle is transformed on impact to radial momentum spreading the ink on the surface. Simultaneously, the impact pressure forces the ink to permeate into the substrate which is also assisted by the capillary effects inherent to the porous substrate. The measured velocities of the impinging drops and the observed supports' porosities combined into a set of dimensionless numbers (*Re, We*) and porous media permeation characteristics which were not suitable for deposition of free-standing coating by DCIJP. The standard printing procedure resulted in seepage of the ink into the metal scaffold. The issue was resolved by implementing printing on heated supports. The elevated temperature of the substrate surface led to partial evaporation of the solvent effectively increasing the viscosity and the surface tension of the landing drops. As a result an increased retention of the ink onto the porous surface was achieved allowing for building of free-standing anode (NiO–GDC) and electrolyte (GDC) coatings with precise control of the thickness. Simultaneously, drops spreading at elevated temperatures can cause enhanced evaporation of the solvent at the periphery of the drop's relics where the thickness of the deposit is relatively thin. The driving force created causes the ink to flow outwards from the centre in order to compensate for the loss of solvent thus forming a thick rim around the perimeter of the drops—the so-called "coffee ring effect" [29]. Such mechanism is detrimental in coatings produced by overlapping of many regularly spaced droplets due to resulting thickness non-uniformity. De Gans et al. [30] exploited the problem by using mixtures of solvents with different vapour pressures and surface tensions in order to induce compensating opposing flows. The evaporation of the high vapour pressure solvent at the contact line created surface tension gradient increasing towards the cooler drop centre and inducing balancing Marangoni flows. Assuming the same approach we experimented with two different diluting solvents in the formulation of our suspension inks. The physical properties of the solvents used in this study are summarized in Table 2 (at 20 °C). Alpha-Terpineol was used as ink carrier and dispersant.

**Table 2** Physical properties of ink carrier and diluting solvents

| | Units | Methanol ($CH_4O$) | 1-Propanol ($C_3H_8O$) | Terpineol ($C_{10}H_{18}O$) |
|---|---|---|---|---|
| Boiling point | °C | 64.60 | 97.40 | 217.00 |
| Density | g/cm$^3$ | 0.79 | 0.80 | 0.9303 |
| Vapour pressure | kPa | 12.88 | 2.10 | 0.30 |
| Surface tension | mN/m | 22.70 | 23.71 | 31.00 |
| Viscosity | mPa·s | 0.59 | 2.25 | 67.00 |

The optimization of drops spreading of composite NiO–GDC–MeOH and NiO–GDC–1-PrOH inks was performed for pressures providing sable jetting at high velocities ($P = 550$ mbar for 1-PrOH; $P = 350$ mbar for MeOH). The porous metal supports temperatures were varied from 100 to 180 °C. Single drops were printed on heated dense 8YSZ electrolyte substrates (Fuel Cell Materials) and the shapes of the relics were analysed with ImageJ software. The values of interest were the diameter, circularity ($C = 4\pi A/p^2$) and roundness ($R = 4A/\pi a^2$), where $A$ is the relic's area, $p$ is the perimeter and $a$ is the major axis of an ellipse fitted to the relic's shape. Circularity and roundness vary over [0,1], higher values being an indicator of a shape

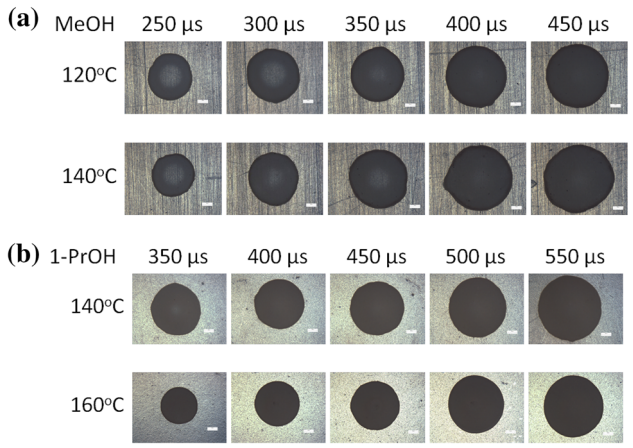


**Fig. 10** Drops relics images deposited at different substrate temperatures and opening times—**a** MeOH- and **b** 1-PrOH-based inks

that is close in character to a perfect circle. The results from the optical analysis can be seen in Figs. 10a,b and 11 a–d. As expected, the droplet diameter increases regularly with opening time, the relation being largely linear and showing varying degrees of "coffee ring effect" with the temperature. The choice of the optimum jetting parameters was a compromise between the necessity of a high productivity of printing (high drop velocity) and high printing resolution (small drop relics diameters and lack of "coffee ring effect"). Hence the optimal printing sets of parameters for both anode composites inks were selected for opening times providing sable jetting and velocities above 1.5 m/s as well as complete absence of any "coffee ring effect". Two candidate sets of parameters were chosen providing high values of circularity and roundness—for MeOH solvent (temperature of 120 °C, and opening time of 400 µs) and for 1-PrOH solvent (temperature of 160 °C, and opening time of 500 µs)—see Fig. 11a–d. The same optimization procedure was repeated for the GDC electrolyte inks.

Figure 12a, b represents cross-sectional images of GDC/NiO–GDC/SS430L fractured half cells fabricated with DCIJP under the optimized conditions and sintered in vacuum. Uniform electrolyte and anode coatings less than 15 µm thick were deposited. It is clear that sintering temperature of 1150 °C was not sufficient for full densification of the electrolyte. The effect of the surface non-uniformity planarization is evident and some infiltration of the anode ink into the stainless steel support can be detected in the area adjacent to the anode/support interface.

## Conclusions

Tape casing and injection moulding techniques were shown to be feasible techniques for the fabrication of 430L stainless steel porous supports. Green planar circular

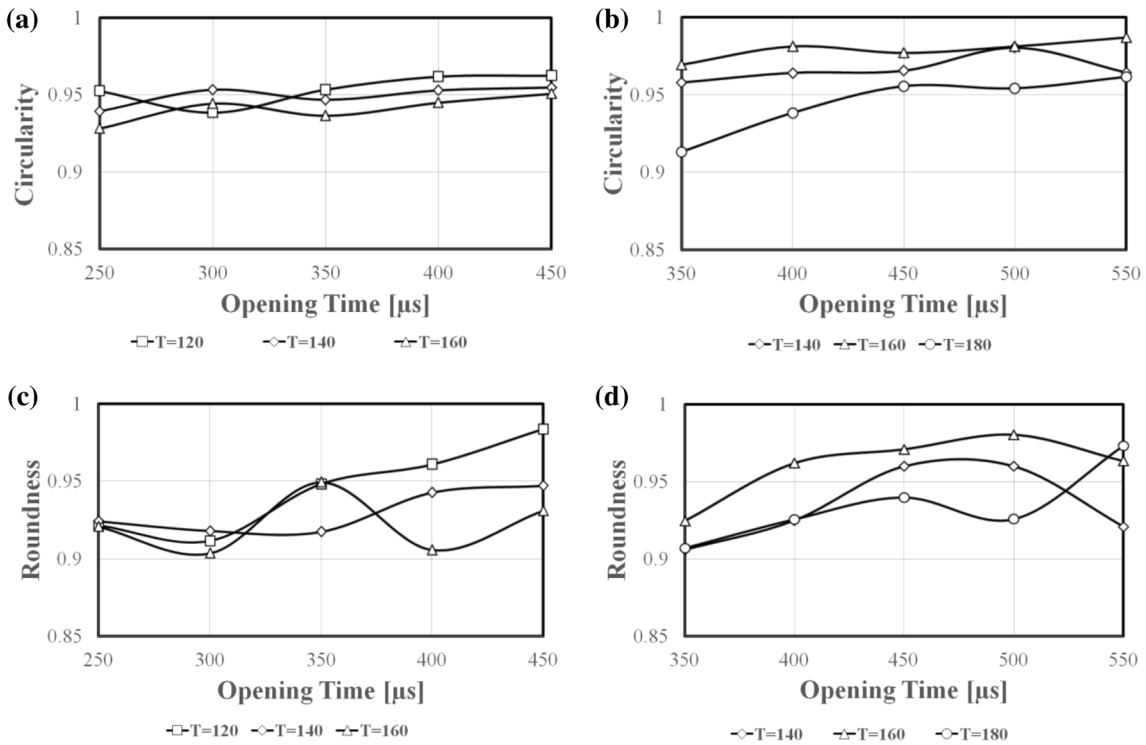


**Fig. 11** Optical analysis of relics images for the circularity **a** MeOH and **b** 1-PrOH and roundness **c** MeOH and **d** 1-PrOH

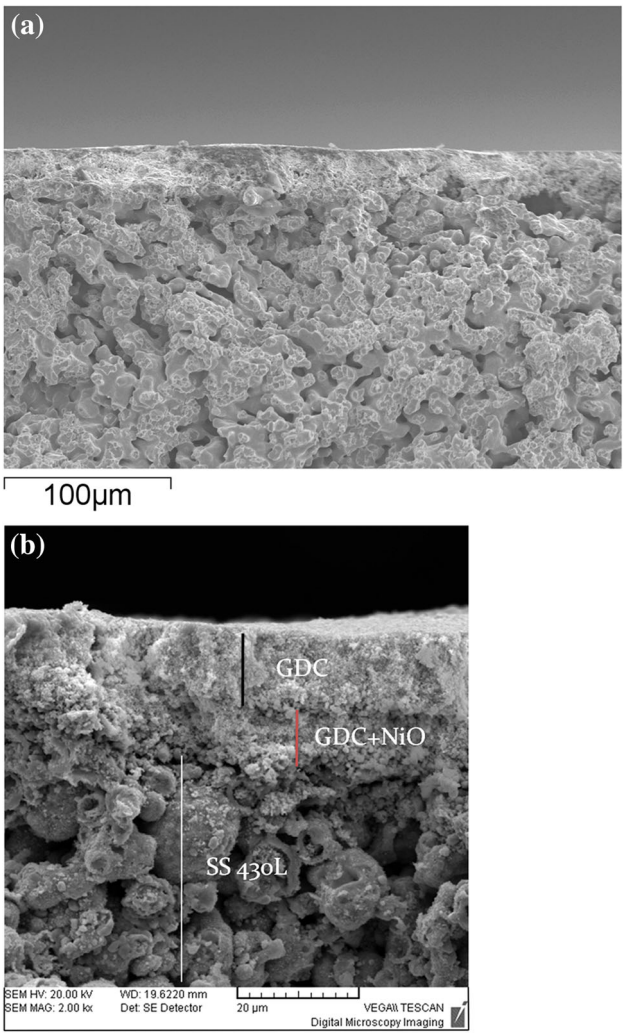


**Fig. 12** Cross-sectional SEM image of fractured half cells inkjet printed on TC stainless steel supports and sintered in vacuum at 1150 °C—(**a**) MeOH ink and (**b**) 1-PrOH ink

supports were produced and sintered in vacuum at different temperatures. The binder removal procedure was done in situ during the sintering cycle. After sintering at 1000 °C the porosity degree of both types of supports was shown to be above 40 %. Vacuum sintering of 430L supports led to skin type enrichment of the stainless steel grains surface to a level of above Cr/Fe wt% ratio of 0.22 which would effectively increase the long-term corrosion resistance under anodic conditions of operation. Direct ceramic inkjet printing on heated supports was successfully employed for production of anode and electrolyte coatings. Optimization of the printing parameters was done by investigation of the drops jetting and spreading behaviour. The effects of inks retention and surface planarization were demonstrated. Anode and electrolyte coatings were deposited on vacuum sintered 430L SS supports under optimized conditions. Cross-sectional images of fractured half cell reveal well-integrated anode and electrolyte coatings less than 15 μm thick. It was found that commonly used sintering temperatures above 1300 °C can cause a complete loss of open porosity. It was also evident that the densification of the electrolyte at 1150 °C was not complete hence further work on utilization of sintering aids is under progress.

**Acknowledgments** The authors wish to acknowledge the EPSRC grant "Performance Optimization of Intermediate Temperature-Solid Oxide Fuel Cells (IT-SOFCs) by Inkjet Printing on Porous Metal Substrates (*JETCELL*)".



## References

1. Singhal, S.: Advances in solid oxide fuel cell technology. Solid State Ion. **135**(1–4), 305–313 (2000)
2. Shao, Z.P., Haile, S.M., Ahn, J., Ronney, P.D., Zhan, Z.L., Barnett, S.A.: A thermally self-sustained micro solid-oxide fuel-cell stack with high power density. Nature **435**, 795–798 (2005)
3. Weber, A.: Ivers-Tiffee, E.: materials and concepts for solid oxide fuel cells (SOFCs) in stationary and mobile applications. J. Power Sources **127**, 273–283 (2004)
4. Gibson, I.R., Dransfield, G.P., Irvine, J.T.S.: influence of yttria concentration upon electrical properties and susceptibility to ageing of yttria-stabilised zirconias. J. Eur. Ceram. Soc. **18**, 661–667 (1998)
5. Jiang, S.P., Chan, S.H.: A review of anode materials development in solid oxide fuel cells. J. Mater. Sci. **39**, 4405–4439 (2004)
6. Singhal, S.C., Kendall, K. (eds.): High Temperature Solid Oxide Fuel Cells: Fundamentals, Design and Applications. Elsevier Ltd, Amsterdam (2003)
7. Kato, H., Kudo, T., Naito, H., Yugami, H.: Electrical conductivity of Al-doped $La_{1-x}Sr_xScO_3$ perovskite-type oxides as electrolyte materials for low-temperature SOFC. Solid State Ion. **159**, 217–222 (2003)
8. Tucker, M.C.: Progress in metal-supported solid oxide fuel cells: a review. J. Power Sources **195**, 4570–4582 (2010)
9. Irvine, J.T.S., Connor, P. (eds.): Solid Oxide Fuels Cells: Facts and Figures. Springer, London (2013)
10. Fergus, J.W.: Metallic interconnects for solid oxide fuel cells. Mater. Sci. Eng. A **397**, 271–283 (2005)
11. Wang, Z., Berghaus, J., Yick, S., Deces-Petit, C., Qu, W., Hui, R., Maric, R., Ghosh, D.: Dynamic evaluation of low-temperature metal-supported solid oxide fuel cell oriented to auxiliary power units. J. Power Sources **176**, 90–95 (2008)
12. Gasik, M. (ed.): Materials for Fuel Cells. Woodhead Publishing and Maney Publishing, Cambridge (2008)
13. Jiang, S.P., Yan, Y. (eds.): Materials for High-Temperature Fuel Cells. Wiley-VCH Verlag GmbH & Co., Weinheim (2013)
14. Piccardo, P., Gannon, P., Chevalier, S., Viviani, M., Barbucci, A., Caboche, G., Amendola, R., Fontana, S.: ASR evaluation of different kinds of coatings on a ferritic stainless steel as SOFC interconnects. Surf. Coat. Technol. **202**, 1221–1225 (2007)

15. Sotomayor, M.E., Ospina, L.M., Levenfeld, B., Várez, A.: Characterization of 430L porous supports obtained by powder extrusion moulding for their application in solid oxide fuel cells. Mater. Charact. **86**, 108–115 (2013)
16. Molin, S., Kusb, B., Gazd, M., Jasinski, P.: Evaluation of porous 430L stainless steel for SOFC operation at intermediate temperatures. J. Power Sources **181**, 31–37 (2008)
17. Elangovan, S., Balagopal, S., Timper, M., Bay, I., Larsen, D., Hartvigsen, J.: Evaluation of Ferritic stainless steel for use as metal interconnects for solid oxide fuel cells. J. Mater. Eng. Perform. **13**(3), 265–273 (2004)
18. Panteix, P.J., Baco-Carles, V., Tailhades, Ph, Rieu, M., Lenormand, P., Ansart, F., Fontaine, M.L.: Elaboration of metallic compacts with high porosity for mechanical supports of SOFC. Solid State Sci. **11**, 444–450 (2009)
19. Williams K.R., Smith, J.G.: Great Britain patent GB 1,049,428 (1966)
20. Ceres Power: Great Britain patents GB 2,368,450, GB 0205291.8, GB 0223316.1, GB 0308215.3, and GB 0308724.4
21. Dobrzański, L.A., Brytan, Z., Grande, M.A., Rosso, M., Pallavicini, E.J.: Properties of vacuum sintered duplex stainless steels. J. Mater. Process. Technol. **162–163**, 286–292 (2005)
22. Bautista, A., Velasco, F., Guzmán, S., de la Fuente, D., Cayuela, F., Morcillo, M.: Corrosion behaviour of powder metallurgical stainless steels in urban and marine environments. Rev Metal **42**(3), 175–184 (2006)
23. Tomov, R.I., Krauz, M., Jewulski, J., Hopkins, S.C., Kluczowski, J.R., Glowacka, D.M., Glowacki, B.A.: Direct ceramic inkjet printing of yttria-stabilized zirconia electrolyte layers for anode-supported solid oxide fuel cells. J. Power Sources **195**, 7160–7167 (2010)
24. Wang, Ch., Hopkins, S.C., Tomov, R.I., Kumar, R.V., Glowacki, B.A.: Optimisation of CGO suspensions for inkjet-printed SOFC electrolytes. J. Eur. Ceram. Soc. **32**, 2317–2324 (2012)
25. Wang, Ch., Tomov, R.I., Kumar, R.V., Glowacki, B.A.: Inkjet printing of gadolinium-doped ceria electrolyte on NiO–YSZ substrates for solid oxide fuel cell applications. J. Mater. Sci. **46**, 6889–6896 (2011)
26. Sukeshini, A.M., Cummins, R., Reitz, T.L., Miller, R.M.: Ink-Jet printing: a versatile method for multilayer solid oxide fuel cells fabrication. J. Am. Ceram. Soc. **92**(12), 2913–2919 (2009)
27. Derby, B.: Inkjet printing of functional and structural materials: fluid property requirements, feature stability, and resolution. Annu. Rev. Mater. Res. **40**, 395–414 (2010)
28. Derby, B.: Inkjet printing ceramics: from drops to solid. J. Eur. Ceram. Soc. **31**, 2543–2550 (2011)
29. Deegan, R.D., Bakajin, O., Dupont, T.F., Huber, G., Nagel, S.R., Witten, T.A.: Contact line deposits in an evaporating drop. Phys. Rev. E **62**(1), 756–765 (2000)
30. De Gans, B.J., Schubert, U.S.: Inkjet printing of well-defined polymer dots and arrays. Langmuir **20**, 7789–7793 (2004)